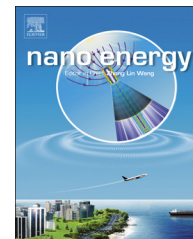




Available online at [www.sciencedirect.com](http://www.sciencedirect.com)

ScienceDirect

journal homepage: [www.elsevier.com/locate/nanoenergy](http://www.elsevier.com/locate/nanoenergy)



RAPID COMMUNICATION

# Micro-sized nano-porous Si/C anodes for lithium ion batteries



Huajun Tian<sup>a</sup>, Xiaojian Tan<sup>a</sup>, Fengxia Xin<sup>a</sup>, Chunsheng Wang<sup>b,\*</sup>,  
Weiqiang Han<sup>a,c,\*\*</sup>

<sup>a</sup>Ningbo Institute of Materials Technology and Engineering, Chinese Academy of Sciences, Ningbo 315201, PR China

<sup>b</sup>Department of Chemical and Biomolecular Engineering, University of Maryland, College Park, MD 20742, USA

<sup>c</sup>School of Physical Science and Technology, Shanghai Tech University, Shanghai 200031, PR China

Received 22 September 2014; received in revised form 2 November 2014; accepted 12 November 2014

Available online 18 November 2014

## KEYWORDS

Lithium-ion batteries;  
Micro-sized;  
Si/C;  
Anode;  
Hierarchical structure

## Abstract

The unique micro-sized (2–10  $\mu\text{m}$ ) Si/C composites consisting of 20 nm carbon coated secondary Si were synthesized from the abundant and low cost Al–Si alloy ingot by acid etching, ball-milling and carbonization procedure. The nano-porous Si/C composites provide a capacity of 1182  $\text{mAh g}^{-1}$  at a current density of 50  $\text{mA g}^{-1}$ , 952  $\text{mAh g}^{-1}$  at 200  $\text{mA g}^{-1}$ , 815  $\text{mAh g}^{-1}$  at 500  $\text{mA g}^{-1}$ , and maintain 86.8% of initial capacity after 300 cycles. Even at a much higher current density of 10 A/g, the porous Si/C anode can still provide capacities of  $>200 \text{ mAh g}^{-1}$ . Its superior rate capability and cycling stability of micro-sized nano-porous Si/C anodes is because it takes advantage of both long cycle life of nano-Si and high volumetric/gravimetric capacity of micro-Si. The hierarchical porous micro-scale Si/C with the carbon coating can stabilize the SEI layer and the inside pore provides adequate space for Si expansion, relaxing the stress/strain. The hierarchical Si/C with exceptional electrochemical performance is prepared by a simple, low-cost and saleable synthesis method, making it very promising for a large-scale production of high-performance Si-based anode materials in high-energy lithium-ion batteries.

© 2014 Elsevier Ltd. All rights reserved.

\*Corresponding author.

\*\*Corresponding author at: Ningbo Institute of Materials Technology and Engineering, Chinese Academy of Sciences, Ningbo 315201, PR China.

E-mail addresses: [cswang@umd.edu](mailto:cswang@umd.edu) (C. Wang),  
[hanweiqiang@nimte.ac.cn](mailto:hanweiqiang@nimte.ac.cn) (W. Han).

## Introduction

The emerging markets of electric vehicles (EV, hybrid EV (HEV) and plug-in hybrid electric vehicles (PHEV)) generate an ever-growing demand for low-cost lithium-ion batteries (LIBs) with high energy and power densities and long cycling

life [1]. The developments of high capacity anode to replace existing carbon-based materials are essential to satisfy the requirement of high energy densities in LIBs for large-scale EV, HEV and PHEV applications.

Lithium-alloying materials (Si, Ge, Sn, Al, Sb, etc.) have much higher Li storage capacity than the commercial carbon-based anode ( $372 \text{ mAh g}^{-1}$ ) [2–16]. Among all the alloy anodes, silicon has the highest specific capacity ( $\sim 3579 \text{ mAh g}^{-1}$ ) at low charge-discharge potentials of  $<0.5 \text{ V}$  (vs.  $\text{Li/Li}^+$ ), corresponding to the formation of the  $\text{Li}_{15}\text{Si}_4$  phase, which delivers 10 times higher theoretical specific capacity than that of a conventional graphite anode [17–23]. Moreover, Si also has a massive volumetric capacity of  $8322 \text{ mAh cm}^{-3}$  [24–28]. However, the use of micro-sized bulk Si is hampered by the pulverization of the Si particles due to high volumetric change of  $\sim 300\%$  during lithiation and delithiation cycles, which leads to particle pulverization and destabilization of a solid electrolyte interphase (SEI) film, thus resulting in fast capacity fading and low Coulombic efficiency [29–31]. One successful method to alleviate mechanical strain induced by volume change of Si is to minimize the particle size of Si into nano-scale [32–35]. However, nano-sized Si with high surface-to-volume ratio increases the irreversible capacity due to the formation of more SEI film. Although the nano-Si will not be pulverized during lithiation/delithiation, the SEI film still continually breaks/reforms, lowering the Coulombic efficiency. Meanwhile, the nano-Si is very expensive due to the costly synthesis process and has low tapping density. The high-cost, low Coulombic efficiency and low tapping density limit the commercialization of nano-Si.

Nanostructuring of micro-scale electrode materials is considered as an effective solution to increase volumetric energy density and reduce the irreversible capacity. Recently, Wang's group successfully prepared porous micro-sized Si-C composite using the  $\text{SiO}$  as the Si source, which demonstrated a high capacity of  $1459 \text{ mAh g}^{-1}$  and retained 97.8% of initial capacity after 200 cycles [36]. The research group at PNNL prepared a large ( $>20 \mu\text{m}$ ) mesoporous silicon sponge by electrochemical etching of single crystal Si wafers, which deliver a capacity of  $\sim 1.5 \text{ mAh cm}^{-2}$  with 92% capacity retention over 300 cycles [37]. Hence, the micro-sized Si with nanoporous structure is very promising for next generation high-energy LIBs. To commercialize the micro-sized nanoporous Si, facile route for mass scale production of the hierarchical micro-sized Si with low cost is necessary.

Cheap Al-Si alloy powders can be used to synthesize porous Si. [38] However, the performance of the porous Si prepared

by simply etching Al out from Al-Si powders is still poor and cannot satisfy the requirement for the practical battery applications. In this study, micro-scaled porous Si particles were prepared by acid etching much cheaper Al-Si alloy ingot ( $\sim \$2500/\text{ton}$ ), which have been widely used as structure materials in the industry. The pore size and distribution of etched porous Si were refined by mechanical milling, and the electronic conductivity and stability of the SEI film were enhanced by applying carbon coating on the surface of the ball milled porous Si. The low-cost hierarchical structured porous Si/C anodes provide  $952 \text{ mAh g}^{-1}$  at  $200 \text{ mA g}^{-1}$ ,  $815 \text{ mAh g}^{-1}$  at  $500 \text{ mA/g}$ ,  $600 \text{ mAh g}^{-1}$  at  $2000 \text{ mA/g}$ , and retain 86.8% of initial capacity after 300 cycles at  $500 \text{ mA g}^{-1}$ , demonstrating one of the best performances for micro-sized low-cost Si. Since the Al-Si alloy ingot is abundant and cheap, the carbon coated micro-sized porous Si with high performance is very promising for practical application.

## Experimental section

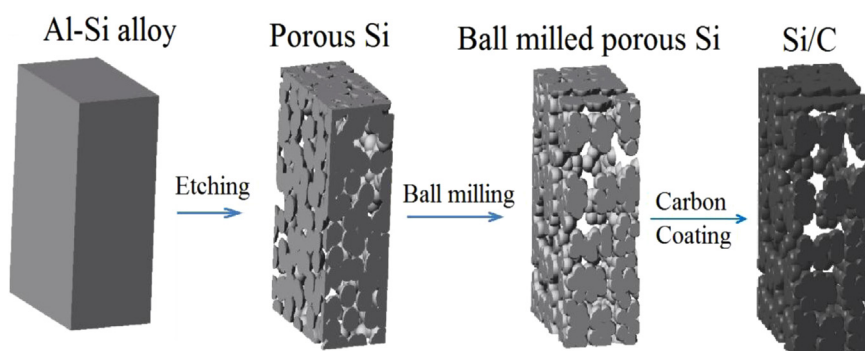
### Material synthesis

#### The preparation of hierarchical micro-sized porous Si

The porous Si using the Al-Si alloy ingot as source was first crushed by the physical method (i.e., lathe, chipping). The size of the Al-Si alloy scraps is  $0.5\text{--}50 \text{ mm}$  (Figure S1). After that, the Al-Si alloy scraps were slowly added into  $5 \text{ wt\%}$  HCl solution with continuous stirring for 10 h in order to remove the aluminum. Then, the rest of the product (porous Si) was washed by deionized water substantially and immersed in  $5\% \text{ HF}$  solution for 8 h to remove the  $\text{SiO}_2$  on the surface of the Si powder. The obtained Si powder was washed sufficiently with ethanol and deionized water and dried in vacuum at  $60^\circ\text{C}$  overnight.

#### The preparation of hierarchical micro-sized porous Si/C

The porous Si and polyacrylonitrile (PAN,  $\text{Mw}=150,000$ , Aldrich) ( $1:1 \text{ wt\%}$ ) were mixed using a ball-mill (PM200, Retsch GmbH Inc., Germany), which is a mature technology for producing harmonious products, operated at a low grinding speed of  $350 \text{ rpm}$  for 24 h in ethanol medium. The mixture of porous Si/PAN was carbonized in a tube furnace at  $700^\circ\text{C}$  for 3 h under  $\text{Ar}$  ( $95 \text{ vol\%}$ )/ $\text{H}_2$  ( $5 \text{ vol\%}$ ) atmosphere with a heating rate of  $10^\circ\text{C/min}$  to obtain the porous Si/C composite material.



**Scheme 1** Schematic illustration of the preparation process from Al-Si alloy to the Si/C composite.

## Structural characterizations

The samples were characterized using scanning electron microscopy (FESEM, FEI QUANTA 250 FEG and FE-SEM, Hitachi, S-4800) and transmission electron microscopy (TEM, FEI Ltd., Tecnai F20). XRD measurements were performed on a D8 diffractometer from Bruker instruments (Cu K $\alpha$  radiation=0.154 nm) equipped with a scintillation counter. The BET specific surface area and pore size distribution were analyzed using N<sub>2</sub> absorption on an ASAP 2020M (Micromeritics Instrument Corp., USA). Thermogravimetric analysis (TGA) was carried out using

Perkin Elmer Diamond TG/DTA instrument at a heating rate of 10 °C min<sup>-1</sup> under air. The X-ray photoelectron spectroscopy (XPS) measurements were carried out on AXIS Ultra DLD systems.

Impurities (mainly including Al and Fe) concentration measurements were performed using Perkin-Elmer Optima 2100 inductively Coupled Plasma-Atomic Emission Spectrometry (ICP-AES).

Raman spectroscopy measurement was conducted with an in Via-Reflex Raman Spectrometer using a 532 nm excitation wavelength using a 50 $\times$  microscope objective at a

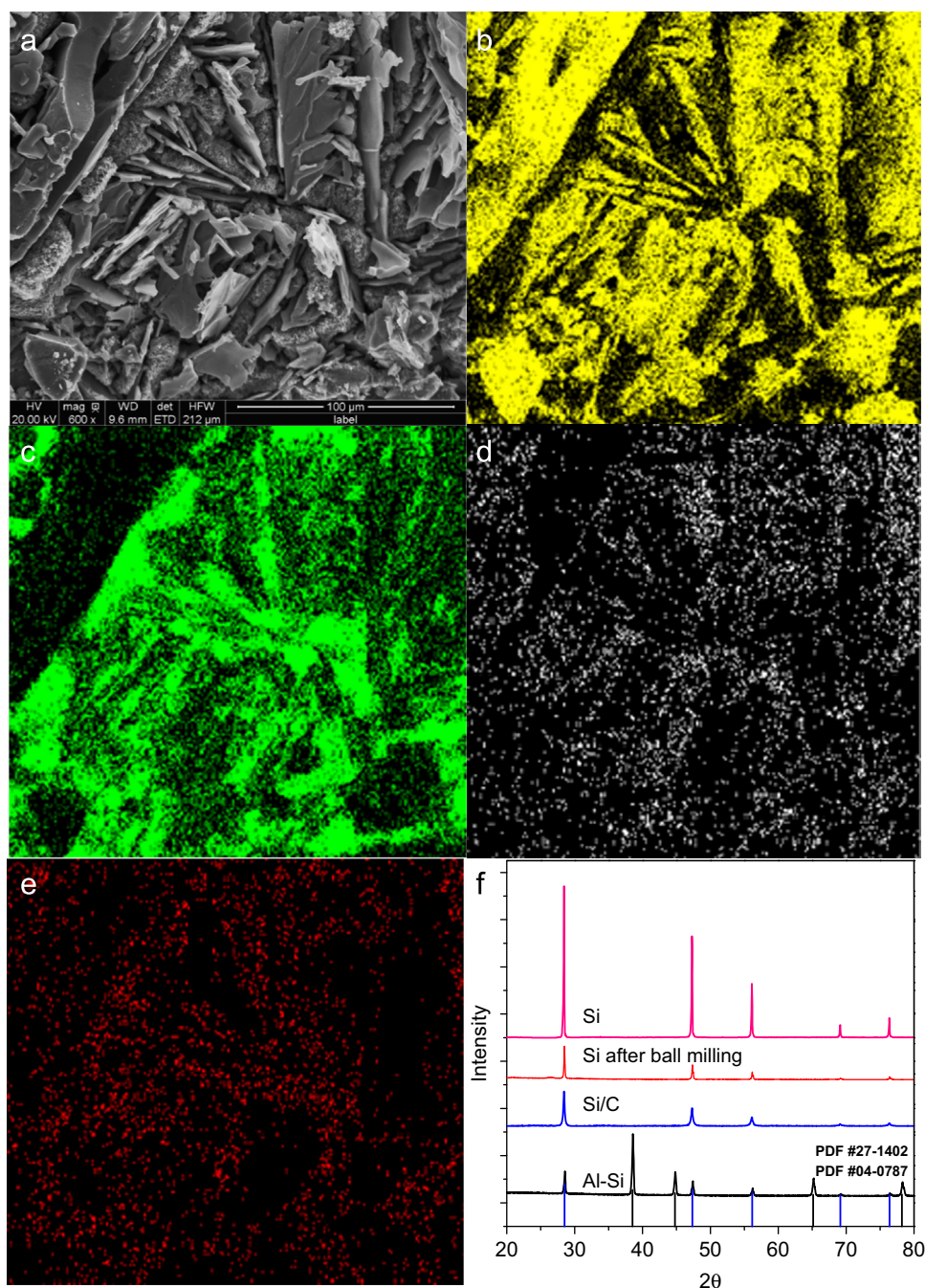


**Figure 1** Characterization of the Al-Si alloy: (a) SEM images of the Al-Si alloy; (b-e) elemental mapping images of the Al-Si alloy inside for silicon (b), aluminum (c), iron (d) and oxygen (e). (f) XRD pattern of Al-Si alloy, etched Si, ball-milled Si and Si/C composite. The diffraction peaks are indexed based on the JCPDS file nos. 00-027-1402 and 00-04-0787.



low laser incident power (0.7 mW). Raman shifts were collected in the range of  $200\text{--}3500\text{ cm}^{-1}$ .

## Electrochemical measurements

Porous Si/C was mixed with Super P carbon black and sodium carboxymethyl cellulose (CMC) binder to form slurry at the weight ratio of 60:20:20. The electrode was prepared by casting the slurry onto copper foil with active material loading of  $\sim 0.5\text{ mg/cm}^2$  using a doctor blade and dried in a vacuum oven at  $120^\circ\text{C}$  overnight. The CR2032 coin cells were assembled with lithium foil as the counter electrode.

$1.0\text{ M LiPF}_6$  solution in a mixture of fluoroethylene carbonate/dimethyl carbonate/ethyl methyl carbonate (FEC/DMC/EMC, 1:1:1 in volume) was used as the electrolyte, and a polypropylene film (Celgard-2300) was used as the separator. The coin cells were assembled in an argon-filled glove box with both moisture and oxygen contents below  $0.1\text{ ppm}$ . The electrochemical properties were studied with a multichannel battery-testing system (BT2000, Arbin Instruments, USA). The cells were discharged and charged galvanostatically in the voltage window from  $0.01$  to  $1.5\text{ V}$  ( $1\text{C}=4000\text{ mA/g}$ ). The capacity was calculated on the basis of the total mass of the Si/C composite active materials. The rate capability was examined by charging, and discharging

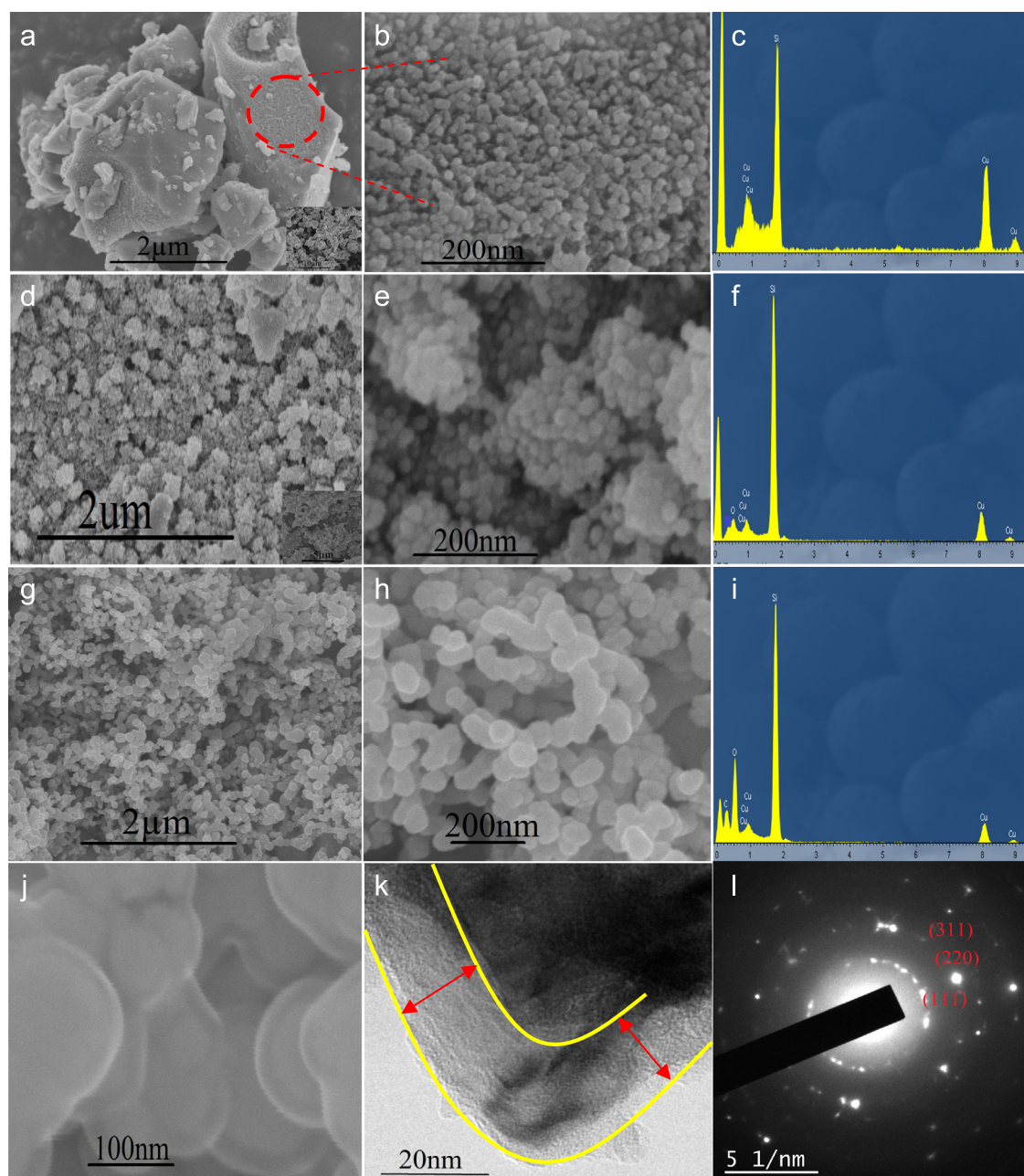


**Figure 2** Typical (a), (b) SEM images and (c) EDS of the prepared etched preliminary Si. (d), (e) SEM images and (f) EDS of ball milled etched Si. (g, h, j) SEM images and (i) EDS of Si/C composite. (k) HRTEM image of Si/C composite, (l) the selected area electron diffraction (SAED) patterns of the core in Si/C.

cells at different rates were calculated based on Si/C composite active materials. Cyclic voltammogram scanned at 0.05 mV/s between 0 and 1.5 V for 10 cycles was recorded using Solartron 1470E Electrochemical Interface (Solartron Analytical, UK). EIS was taken using a Solartron 1470E Electrochemical Interface (Solartron Analytical, UK) electrochemical workstation at 25 °C with the frequency ranging from 1 MHz to 0.001 Hz and an AC signal of 10 mV in amplitude as the perturbation.

## Results and discussion

### Morphology and structure of porous Si/C

The synthesis process of the Si/C composite is schematically summarized in Scheme 1, and illustrated in detail in Figure S1. The Al-Si scraps can be easily crushed from brittle Al-20% Si ingot. The Al-Si scraps consist of a small amount of primary crystals silicon and a large amount of eutectic Si-Al matrix (Figure 1a). The primary silicon sheets are sandwiched in Al matrix as demonstrated in the EDS of Al and Si element mapping in Figure 1b and c. Small amounts of Fe and O exist in Al-Si alloys (Figure 1d and e). The XRD pattern in Figure 1f shows that Al and Si in Al-Si alloys are in crystal structures. The region with Al and Si overlap is the eutectic Si-Al matrix (Figure 1b and c). We attribute the success of preparing micro-sized porous Si particles through a simple etching of Si-Al matrix and the selection of the etchant components.

Figure 2a,b presents the electron microscope images of micro-sized porous eutectic Si after the Al was etched out. The size of primary eutectic Si is 2–10  $\mu\text{m}$ , consisting of  $\sim 20$  nm

secondary Si and  $\sim 15$  nm pores. XRD in Figure 1f confirmed that Al was basically removed from micro-sized Al-Si powders (JCPDS Card no.27-1402), which is also confirmed by the energy dispersive X-ray spectra (EDS) (Figure 2c). The obtained porous-Si is in a single crystal, as demonstrated in Figure S2. The lattice fringe with an interlayer distance of 0.314 nm agrees well with the spacing between (111) planes of Si crystals.

After acid etching, impurity concentrations of the prepared preliminary Si were measured using an inductively coupled plasma atomic emission spectrometer (ICP-AES), showing the main impurity concentrations of Al and Fe being 0.13 wt% and

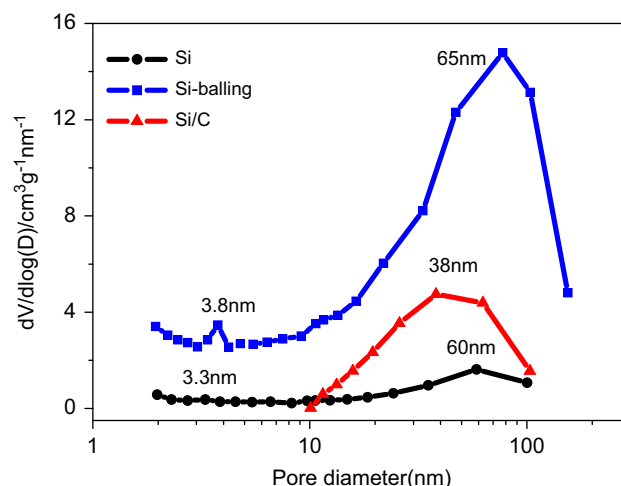


**Figure 4** Pore size distribution of the prepared preliminary Si, ball-milled Si and Si/C composite.

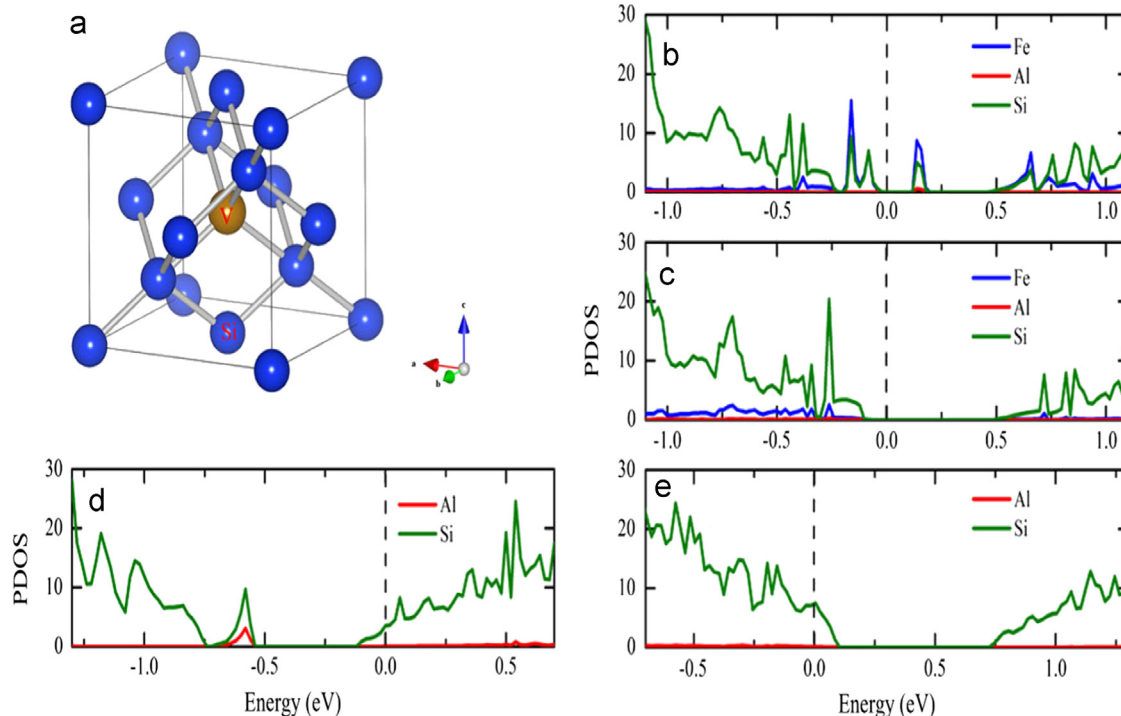


**Figure 3** (Color online) The whole atomic is a cubic  $3 \times 3 \times 3$  supercell in first-principle calculations, (a) is part of the atomic model for doped silicon, and (b), (c), (d), and (e) are the atom-projected density of states (PDOS) for Al, Fe codoping spin-up state, spin-down state, Al substituting the Si site (Si), and Al occupying the vacancy site (V), respectively.

0.06 wt%, respectively. If traces of Al and Fe are doped in the Si, it will increase the electronic conductivity, thus enhancing the lithiation/delithiation reaction kinetics. The mechanism of conductivity enhancement for Al and Fe doping in Si was investigated using the first-principle calculations. As shown in Figure 3a, there are two sites for Al, Fe doping: silicon site (Si) and vacancy site (V). Al, Fe tend to codope silicon and form Al-Fe pairs (Al substituting the Si site and Fe occupying the vacancy site) [39]. Thus, Fe would mainly exhibit the Fe-Al codoping pairs in our silicon sample. Oswald et al. reported that the peak of the Si 2p in Al doped Si only shifts from 99.5 eV to 99.6 eV due to very small amount of Al implantation, while the Al 2p peak shifts to 73.3 eV due to high Al-Si binding energy [40]. As shown in Figure S3a, the peak of Al 2p is located at 73.6 eV, demonstrating the existence of Al-Si binding in the etched Si sample. Figure S3b shows that the main Si peak of the Si 2p is located around 99.5 eV. The existence of Al and Fe residues in etched Si sample was confirmed by ICP-AES measurement. Vankooten et al. also pointed out that Al, Fe tend to codope silicon and form Al-Fe pairs [39]. Considered Fe is 3d transition metal, we compared the energy for the nonmagnetic (NM) states and ferromagnetic (FM) states of Al-Fe codoped silicon and found the total energy of FM states is 0.6 eV lower than the NM states. Figure 3b and c shows the corresponding PDOS for spin-up and spin-down state of Al-Fe codoped silicon, respectively. It can be seen that the spin-up state exhibits obvious impurity states near the Fermi level and the activation energy is about 0.2 eV, while the spin-down state affects less the edges of the Fermi level for doped silicon. The emerging impurity excitation is more favorable to increase the carrier concentration than intrinsic excitation, leading to higher electrical conductivity. On the other hand, the Al content is much higher than that of Fe, and the excessive Al atoms would form other point defects in the doped silicon sample. The PDOS of Al substituting the Si site and Al occupying the vacancy site are plotted in Figure 3d and e. Al substituting the Si site and Al occupying the vacancy site would move the Fermi level toward the conduction bands and valence bands, respectively, which could increase the electron/hole concentration in systems, although no impurity states are introduced. Another benefit for partial Al-doping is that it can effectively prevent expanding of Si lattice (C (~10%), Al (~94%) and Si (~280% for amorphous Si), respectively, due to their different Li

uptake capacities) [41]. Therefore, the low concentration Fe and Al impurities can increase the electrical conductivity, reduce the lattice expansion of silicon sample, and improve the performance of Si as anode materials in LIBs.

The porous Si formed by etching Al-Si alloys normally shows poor cycling stability, due to the weak connection between Si dendrite in micro-sized porous Si [38]. To increase the connection between the Si particles in porous Si, the porous Si was ball milled for 24 h. As shown in Figure 2d-f, the ~2  $\mu\text{m}$  porous Si (Figure 2d and e) aggregates into 5  $\mu\text{m}$  primary Si particles that consist of 200 nm nano-Si cluster formed by ~20 nm Si particles. The nano-Si and nano-Si cluster are well connected with each other, which improves the cycling stability. Meanwhile, the ball milling for 24 h significantly increases the surface area of porous Si from 1.8  $\text{m}^2/\text{g}$  to 37  $\text{m}^2/\text{g}$  and pore volume from 0.018  $\text{cm}^3/\text{g}$  to 0.138  $\text{cm}^3/\text{g}$  but only slightly increases the pore size from 60 nm to 65 nm as demonstrated in the BET measurement (Figure 4, Figure S4 in support information), which will increase the rate performance. The ball milling also changes the single crystal porous Si into partially amorphous Si as evidenced by the slope first lithiation curve [42].

Carbon coating on the micro-sized porous Si can greatly increase the rate performance and cycling stability [36,43]. To uniformly coat carbon on the surface of porous Si, PAN polymer was ball milled with etched porous Si for 24 h, and then carbonized at 700  $^{\circ}\text{C}$  in Ar (95 vol%)/ $\text{H}_2$  (5 vol%) atmosphere for 3 h. The SEM and TEM images of Si/C composite are illustrated in Figure 2g-l. As shown in Figure 2j and k, a layer of carbon with a thickness of 15 nm is uniformly coated on the nano-Si surface. The STEM EDS elemental mapping images in Figure 5 also clearly demonstrate that the Si nanoparticle is coated by a uniform layer of amorphous carbon. The SAED in the Si spot (Figure 2l) shows the discontinuous diffraction rings correspond to (111), (220), and (311) planes of Si. TGA measurement shows that the amount of carbon coating on Si is 25% by weight (Figure S5 in support information). The nature of C coating and Si in the Si/C composite was investigated by Raman spectroscopy (Figure S6 in support information). The peak at ~520  $\text{cm}^{-1}$  corresponds to the characteristic band of single crystalline silicon, confirming the presence of crystal silicon in the samples [44]. The peaks appearing at about 1350, 1590, and 2700  $\text{cm}^{-1}$  are assignable

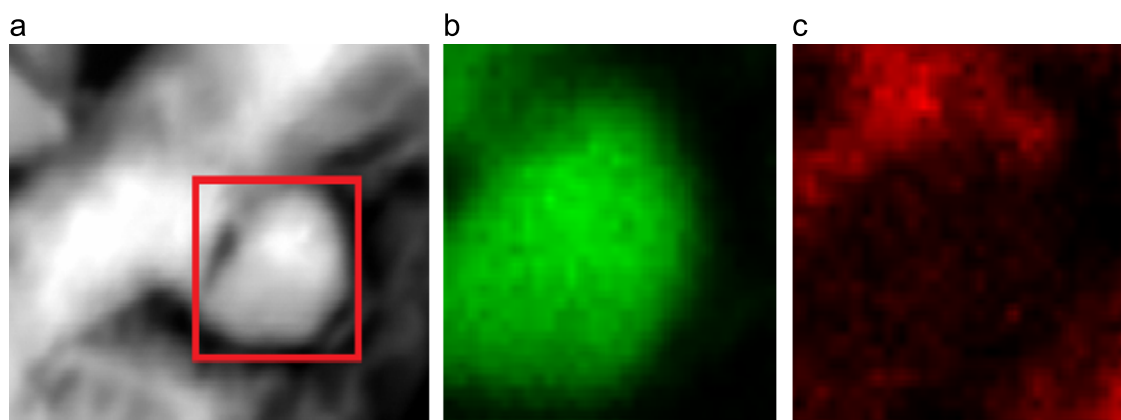


**Figure 5** TEM image of Si/C composites (a) and EDS elemental mapping images of the Si/C composites, marked by red square, for silicon (b) and carbon (c).

as the D, G and 2D bands of carbon, respectively [45]. The relatively higher intensity of D band than that of G-band mainly results from the defects and partially disordered structure of the coating carbon. After carbon coating, the BET surface decreased from  $37.0 \text{ m}^2 \text{ g}^{-1}$  for ball milled Si to  $21.4 \text{ m}^2 \text{ g}^{-1}$  for Si/C composite, while the pore size decreased from 65 nm to 38 nm (Figure 4), indicating that carbon was effectively coated inside the pores.

### Electrochemical performance of porous Si/C

Figure 6a shows the cyclic voltammogram (CV) of Si/C composite. In the first cathodic (lithiation) scan, the small and broad peak located at 0.6 V (vs.  $\text{Li}/\text{Li}^+$ ) is attributed to the formation of solid electrolyte interphase (SEI) film, which leads to irreversible capacity loss and low Coulombic efficiency in the first cycle [46]. Moreover, only one peak at  $\sim 0 \text{ V}$

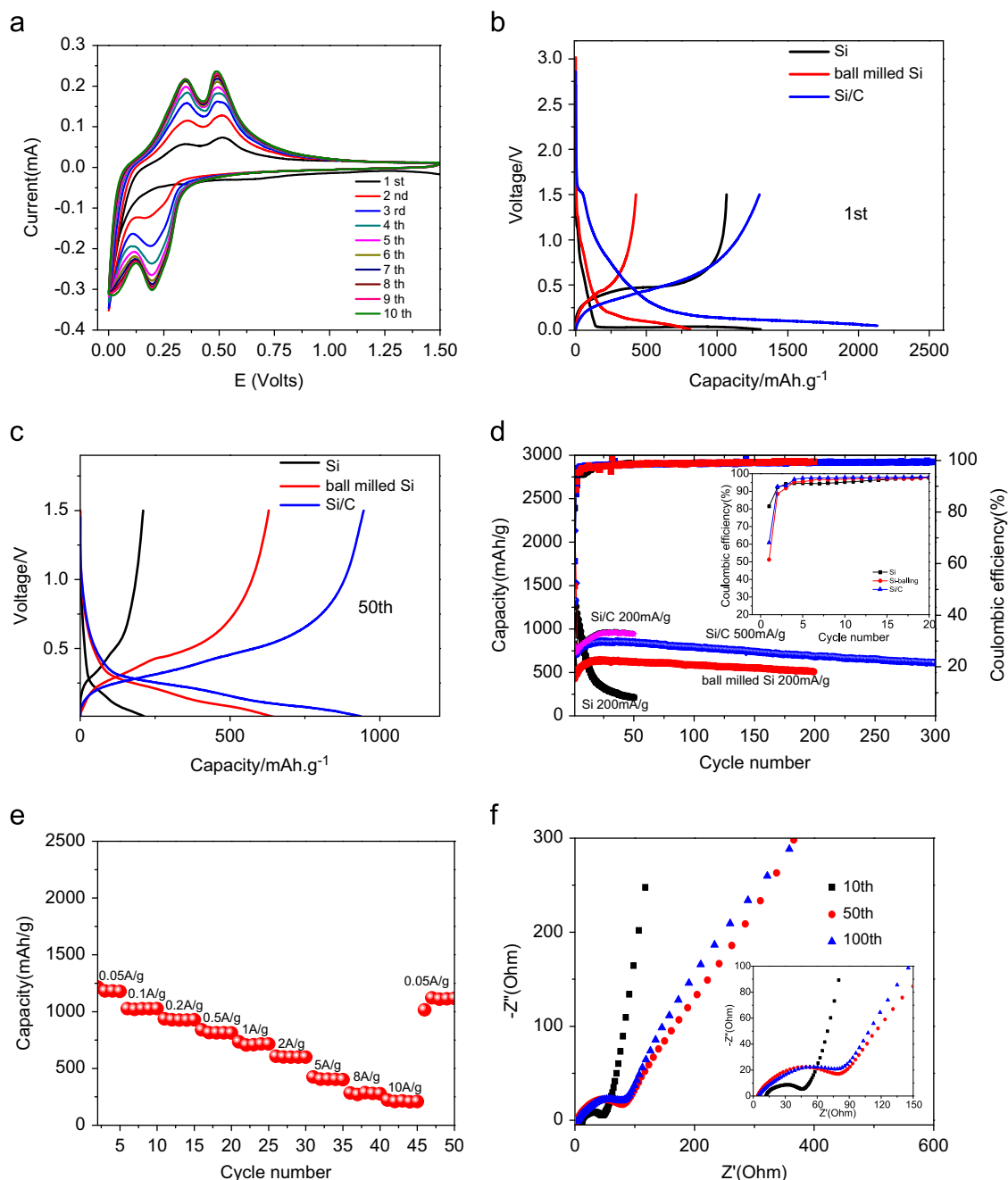


**Figure 6** Electrochemical characterizations of the synthesized porous Si, ball milled Si and Si/C composite. (a) Cyclic voltammograms of the Si/C composite in the initial ten cycles. (b) charge/discharge profiles of Si/C composite at the 1st cycle; (c) charge/discharge profiles of Si/C composite at the 50th cycle; (d) charge–discharge cycling test of Si, ball milled Si and Si/C electrodes at a current density of 0.2 A/g and 0.5 A/g. (e) Capacity retention of Si/C composite. (f) Nyquist plots of the electrodes of Si/C anode after 10th, 50th and 100th charge/discharge cycles at the 500 mA/g current density (inset is the enlarged EIS plot in high-frequency region), obtained after charging the Si/C anode to 1.5 V and relaxation for 2 h.



is observed in the first cathodic scan, representing the lithiation process of the crystalline Si. During the following anodic and cathodic scans, the cathodic peaks at  $\sim 0.20$  V and  $0.01$  V and anodic peaks at  $0.32$  V and  $0.51$  V are observed, which are the typical behaviors of Li alloying/dealloying with amorphous Si [47]. Meanwhile, a broad cathodic peak at  $\sim 0.20$  V and the anodic peaks at  $\sim 0.32$  and  $0.51$  V gradually increase with charge/discharge cycles due to activation of the hierarchical micro-sized crystal Si, which has been reported in porous Si [5,47,48].

All the electrodes were galvanically charged/discharged at a rate of  $C/80$  ( $50 \text{ mA g}^{-1}$ ) for the first 2 cycles and then cycled at a high rate ( $200 \text{ mA g}^{-1}$ ) for all subsequent cycles. The first and 50th charge/discharge curves of etched porous Si, ball milled porous Si and ball milled porous Si with carbon coating at  $50 \text{ mA g}^{-1}$  ( $50^{\text{th}}$  charge/discharge curve at  $200 \text{ mA g}^{-1}$ ) are shown in Figure 6b and c. The specific capacities in Figure 6 are based on the total weight of the Si/C composite. The etched porous Si shows a very flat lithiation plateau of crystal Si and delivers initial discharge and charge capacities of  $1309$  and  $1067 \text{ mAh/g}$ , respectively, corresponding to a first cycle Coulombic efficiency (CE) of  $81.5\%$ . The first lithiation curves of ball milled porous Si and milled porous Si with carbon coating show the behavior of amorphous Si. The ball milling of porous Si reduces the first cycle capacity, but the following carbon coating on ball milled porous Si greatly increases the first cycle capacity. After 50 cycles, the capacity of etched porous Si quickly decreases to  $210 \text{ mAh g}^{-1}$ , while the capacities of ball milled porous Si increase to  $651 \text{ mAh g}^{-1}$ , and of ball milled Si/C composite even reach  $952 \text{ mAh g}^{-1}$  (Figure 6c). However, the ball milling decreases the first cycle Coulombic efficiency of porous Si from  $81.5\%$  to  $51\%$  due to the increase in surface area. In addition, carbon coating increases the CE back to  $61\%$ . The large first cycle irreversible capacity loss due to the formation of SEI on the carbon surface can be solved by performing prelithiation of the Si/C composite [3,37]. The Coulombic efficiency of the carbon coated porous Si/C anode reaches  $99.4\%$  after 4 cycles and remains relatively stable ( $>99.4\%$ ) in subsequent cycles (inset of Figure 6d). Figure 6d shows the cycle performance of the porous Si, ball milled porous Si and ball

milled porous Si/C composite. The ball-milled Si anodes can maintain a capacity of  $\sim 511 \text{ mAh g}^{-1}$  at  $200 \text{ mA g}^{-1}$  after 200 full charge and discharge cycles. The capacity retention is  $94.9\%$  of initial capacity at  $200 \text{ mA g}^{-1}$ , with an average loss over 200 cycles of only  $0.025\%$  per cycle. Carbon coating on ball milled Si not only enhances the capacity from  $651 \text{ mAh g}^{-1}$  to  $952 \text{ mAh g}^{-1}$ , but also maintains the high capacity retention rate over 50 cycles at  $200 \text{ mA g}^{-1}$ .

To examine the long term cycling stability, the ball milled porous Si anodes with carbon coating were charged/discharged at a higher rate of  $500 \text{ mA g}^{-1}$  for 300 cycles. The capacity retention of Si-C composite is  $96.4\%$  from the 3rd to 200th cycle, with an average loss over 200 cycles of only  $0.018\%$  per cycle. After 300 cycles, the capacity retention of Si-C composite is  $86.8\%$ , demonstrating one of the best performances among the micro-sized Si reported to date (Supporting information Table S1). The Si/C composite anode also shows high rate performance (Figure 6e). The Si/C composite anode provides capacity of  $1182 \text{ mAh g}^{-1}$  at a current density of  $50 \text{ mA g}^{-1}$ ,  $815 \text{ mAh g}^{-1}$  at  $500 \text{ mA g}^{-1}$  and  $600 \text{ mAh g}^{-1}$  at  $2 \text{ A/g}$ . Even at a high current density of  $5 \text{ A/g}$ , the specific capacity is  $406 \text{ mAh g}^{-1}$  still higher than the theoretical capacity of graphite ( $\sim 372 \text{ mAh g}^{-1}$ ). At a much higher current density of  $10 \text{ A/g}$ , (i.e., charge/discharge rate of  $2.5 \text{ C}$ ), porous Si/C anode can still provide capacities of  $>200 \text{ mAh g}^{-1}$ . Most importantly, a capacity of  $1120 \text{ mAh g}^{-1}$  at  $50 \text{ mA g}^{-1}$  is retained after 50 cycles of charge and discharge at various current densities (Figure 6e), indicating excellent cycling stability.

To further understand the origin of the superior rate performance of the Si/C composite anode, electrochemical impedance spectra (EIS) were carried out to analyze the resistance evolution of the Si/C composite anode during cycles. The Nyquist plots of porous Si/C composite at the fully delithiated state (charge to  $1.5 \text{ V}$ ) at the 10th, 50th, and 100th cycles are shown in Figure 6f. The high-frequency semicircle in EIS stands for interface (SEI and charge transfer) impedance of Si/C particles, while the low-frequency line represents ion diffusion resistance in the Si/C anode [49]. In Figure 6f, the interfacial resistance increases from 10th to 50th cycles and then maintains the resistance to 100 cycles, indicating an excellent structural stability of the electrode

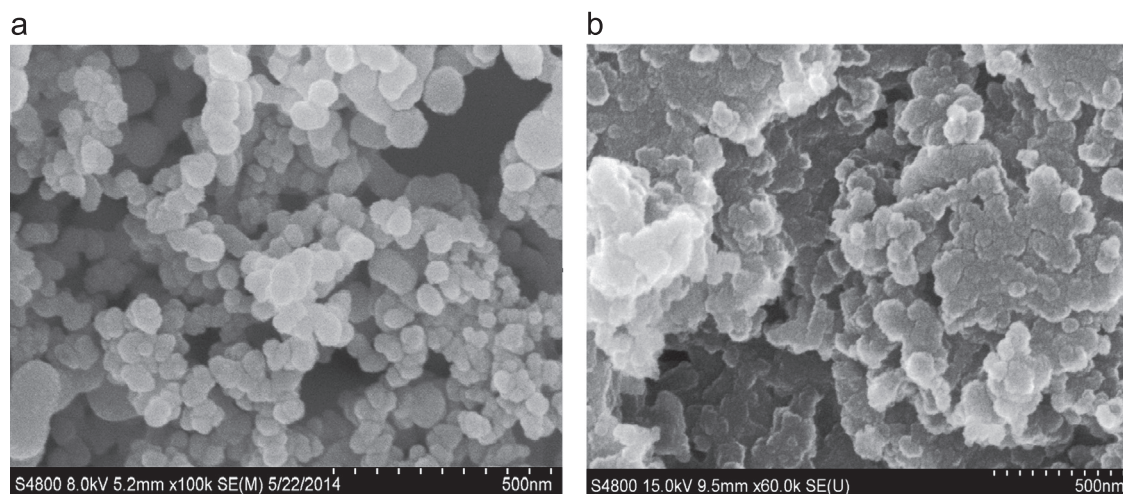


**Figure 7** SEM of the Si/C composite (a) before and (b) after 200 fully charge/discharge circles at a current density of  $0.5 \text{ A/g}$ .



materials as well as a good electronic contact between the active materials and the current collector. These EIS results are in good agreement with the charge/discharge cycling performance (Figure 6d) and the SEM observations (Figure 7). In Figure 7, the fresh Si/C composite electrode shows aggregated porous Si structure. After 200 cycles, the Si/C composite electrode still maintains porous Si structure except a thin SEI layer is coated on the porous Si particles. Moreover, the low and stable resistance of SEI layer and charge transfer reaction is coincident with the exceptional rate capability of the Si/C composite (Figure 6e), demonstrating its fast kinetics.

## Conclusion

In conclusion, we fabricated hierarchical micro-sized porous Si/C composite materials as high-performance Li-ion battery anodes using a low-cost scalable synthesis route by acid etching, ball-milling and carbon coating the abundant, cheap Al-Si alloy ingot, which has been widely used as structure material in the industry. The hierarchical micro-sized Si/C composite anodes consisting of carbon coated nano-scale porous Si units can take advantage of both long cycle life of nano-Si and high volumetric/gravimetric capacity of micro-Si. The hierarchical porous micro-scale Si/C with the carbon coating can stabilize the SEI layer, and the inside pore provides adequate space for Si expansion, relaxing the stress/strain. The unique micro-size Si/C particle with nano-scaled pore and Si structure provides high overall capacity of  $\sim 1200 \text{ mAh g}^{-1}$  at a current density of  $50 \text{ mA g}^{-1}$ , maintains 86.8% of initial capacity after 300 cycles at the current density of  $500 \text{ mA g}^{-1}$ , with an average loss of only 0.044% per cycle, demonstrating one of the best performances for micro-sized low-cost Si. These results would promote the practical application of Si/C composite materials as high capacity electrode with high rate capability for next generation LIBs.

## Acknowledgments

This work was financially supported by the “Strategic Priority Research Program” of the Chinese Project Academy of Science (Grant no. XDA01020304), the National Natural Science Foundation of China (Grant no. 51371186), Zhejiang Province Preferential Postdoctoral Funded Project (No. BSH1302055), Ningbo 3315 International Team of Advanced Energy Storage Materials, and Ningbo Natural Science Foundation (Grant No. 2014A610046), Zhejiang Province Key Science and Technology Innovation Team (2013PT16).

## Appendix A. Supporting information

Supplementary data associated with this article can be found in the online version at <http://dx.doi.org/10.1016/j.nanoen.2014.11.031>.

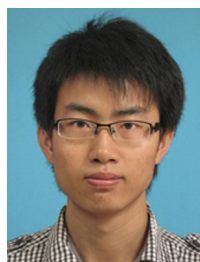
## References

- [1] M. Armand, J.M. Tarascon, *Nature* 451 (2008) 652–657.
- [2] Q.Z. Xiao, Q. Zhang, Y. Fan, X.H. Wang, R.A. Susantyoko, *Energ Environ. Sci.* 7 (2014) 2261–2268.
- [3] N. Liu, H. Wu, M.T. McDowell, Y. Yao, C.M. Wang, Y. Cui, *Nano Lett.* 12 (2012) 3315–3321.
- [4] D.J. Xue, S. Xin, Y. Yan, K.C. Jiang, Y.X. Yin, Y.G. Guo, L.J. Wan, *J. Am. Chem. Soc.* 134 (2012) 2512–2515.
- [5] M.Y. Ge, J.P. Rong, X. Fang, C.W. Zhou, *Nano Lett.* 12 (2012) 2318–2323.
- [6] X.L. Wang, W.Q. Han, H.Y. Chen, J.M. Bai, T.A. Tyson, X.Q. Yu, X.J. Wang, X.Q. Yang, *J. Am. Chem. Soc.* 133 (2011) 20692–20695.
- [7] Y.H. Xu, Q. Liu, Y.J. Zhu, Y.H. Liu, A. Langrock, M.R. Zachariah, C.S. Wang, *Nano Lett.* 13 (2013) 470–474.
- [8] Y.H. Xu, Y.J. Zhu, Y.H. Liu, C.S. Wang, *Adv. Energy Mater.* 3 (2013) 128–133.
- [9] M.S. Park, G.X. Wang, Y.M. Kang, D. Wexler, S.X. Dou, H.K. Liu, *Angew. Chem. Int. Ed.* 46 (2007) 750–753.
- [10] M.J. Lindsay, G.X. Wang, H.K. Liu, *J. Power Sources* 119 (2003) 84–87.
- [11] M.D. Fleischauer, M.N. Obrovac, J.R. Dahn, *J. Electrochem. Soc.* 155 (2008) A851–A854.
- [12] J.M. Mosby, A.L. Prieto, *J. Am. Chem. Soc.* 130 (2008) 10656–10661.
- [13] H. Bryngelsson, J. Eskhult, L. Nyholm, M. Herranen, O. Alm, K. Edstrom, *Chem. Mater.* 19 (2007) 1170–1180.
- [14] A. Darwiche, C. Marino, M.T. Sougrati, B. Fraisse, L. Stievenot, J. Monconduit, *J. Am. Chem. Soc.* 134 (2012) 20805–20811.
- [15] K. Wang, X.M. He, J.G. Ren, L. Wang, C.Y. Jiang, C.R. Wan, *Electrochim. Acta* 52 (2006) 1221–1225.
- [16] B. Liu, X.F. Wang, H.T. Chen, Z.R. Wang, D. Chen, Y.B. Cheng, C.W. Zhou, G.Z. Shen, *Sci. Rep.* 3 (2013) 1622.
- [17] X.H. Liu, H. Zheng, L. Zhong, S. Huan, K. Karki, L.Q. Zhang, Y. Liu, A. Kushima, W.T. Liang, J.W. Wang, J.H. Cho, E. Epstein, S.A. Dayeh, S.T. Picraux, T. Zhu, J. Li, J.P. Sullivan, J. Cumings, C.S. Wang, S.X. Mao, Z.Z. Ye, S.L. Zhang, J.Y. Huang, *Nano Lett.* 11 (2011) 3312–3318.
- [18] B.C. Yu, Y. Hwa, C.M. Park, J.H. Kim, H.J. Sohn, *RSC Adv.* 3 (2013) 9408–9413.
- [19] M.L. Terranova, S. Orlanducci, E. Tamburri, V. Guglielmotti, M. Rossi, *J. Power Sources* 246 (2014) 167–177.
- [20] Y.H. Xu, Y.J. Zhu, C.S. Wang, *J. Mater. Chem. A* 2 (2014) 9751–9757.
- [21] S. Yoo, J.I. Lee, M. Shin, S. Park, *ChemSusChem* 6 (2013) 1153–1157.
- [22] J.S. Bridel, T. Azais, M. Morcrette, J.M. Tarascon, D. Larcher, *Chem. Mater.* 22 (2010) 1229–1241.
- [23] R. Yi, J.T. Zai, F. Dai, M.L. Gordin, D.H. Wang, *Nano Energy* 6 (2014) 211–218.
- [24] Y.H. Xu, J.C. Guo, C.S. Wang, *J. Mater. Chem.* 22 (2012) 9562–9567.
- [25] Y. Oumellal, N. Delpuech, D. Mazouzi, N. Dupre, J. Gaubicher, P. Moreau, P. Soudan, B. Lestriez, D. Guyomard, *J. Mater. Chem.* 21 (2011) 6201–6208.
- [26] D. Reyter, S. Rousselot, D. Mazouzi, M. Gauthier, P. Moreau, B. Lestriez, D. Guyomard, L. Roue, *J. Power Sources* 239 (2013) 308–314.
- [27] X.L. Chen, K. Gerasopoulos, J.C. Guo, A. Brown, C.S. Wang, R. Ghodssi, J.N. Culver, *ACS Nano* 4 (2010) 5366–5372.
- [28] F. Wang, L.J. Wu, B. Key, X.Q. Yang, C.P. Grey, Y.M. Zhu, J. Graetz, *Adv. Energy Mater.* 3 (2013) 1324–1331.
- [29] H. Wu, G. Chan, J.W. Choi, I. Ryu, Y. Yao, M.T. McDowell, S.W. Lee, A. Jackson, Y. Yang, L.B. Hu, Y. Cui, *Nat. Nanotechnol.* 7 (2012) 309–314.
- [30] J.H. Cho, S.T. Picraux, *Nano Lett.* 14 (2014) 3088–3095.
- [31] M.Y. Nie, D.P. Abraham, Y.J. Chen, A. Bose, B.L. Lucht, *J. Phys. Chem. C* 117 (2013) 13403–13412.
- [32] A.S. Arico, P. Bruce, B. Scrosati, J.M. Tarascon, W. Van Schalkwijk, *Nat. Mater.* 4 (2005) 366–377.

- [33] A. Odani, A. Nimberger, B. Markovsky, E. Sominski, E. Levi, V.G. Kumar, A. Motiei, A. Gedanken, P. Dan, D. Aurbach, *J. Power Sources* 119 (2003) 517-521.
- [34] P.G. Bruce, B. Scrosati, J.M. Tarascon, *Angew. Chem. Int. Ed.* 47 (2008) 2930-2946.
- [35] X.H. Liu, L. Zhong, S. Huang, S.X. Mao, T. Zhu, J.Y. Huang, *ACS Nano* 6 (2012) 1522-1531.
- [36] R. Yi, F. Dai, M.L. Gordin, S.R. Chen, D.H. Wang, *Adv. Energy Mater.* 3 (2013) 295-300.
- [37] X.L. Li, M. Gu, S.Y. Hu, R. Kennard, P.F. Yan, X.L. Chen, C.M. Wang, M.J. Sailor, J.G. Zhang, J. Liu, *Nat. Commun.* (2014).
- [38] Z.Y. Jiang, C.L. Li, S.J. Hao, K. Zhu, P. Zhang, *Electrochim. Acta* 115 (2014) 393-398.
- [39] J.J. Vankooten, G.A. Weller, C.A.J. Ammerlaan, *Phys. Rev. B* 30 (1984) 4564-4570.
- [40] S. Oswald, H. Wirth, *Surf. Interface Anal.* 27 (1999) 136-141.
- [41] R. Krishnan, T.M. Lu, N. Koratkar, *Nano Lett.* 11 (2011) 377-384.
- [42] U. Kasavajjula, C.S. Wang, A.J. Appleby, *J. Power Sources* 163 (2007) 1003-1039.
- [43] R. Yi, F. Dai, M.L. Gordin, H. Sohn, D.H. Wang, *Adv. Energy Mater.* 3 (2013) 1507-1515.
- [44] D.M. Piper, T.A. Yersak, S.B. Son, S.C. Kim, C.S. Kang, K.H. Oh, C.M. Ban, A.C. Dillon, S.H. Lee, *Adv. Energy Mater.* 3 (2013) 697-702.
- [45] Y.C. Ru, D.G. Evans, H. Zhu, W.S. Yang, *RSC Adv.* 4 (2014) 71-75.
- [46] S.M. Zhu, C.L. Zhu, J. Ma, Q. Meng, Z.P. Guo, Z.Y. Yu, T. Lu, Y. Li, D. Zhang, W.M. Lau, *RSC Adv.* 3 (2013) 6141-6146.
- [47] F.M. Hassan, V. Chabot, A.R. Elsayed, X.C. Xiao, Z.W. Chen, *Nano Lett.* 14 (2014) 277-283.
- [48] H.C. Tao, L.Z. Fan, X.H. Qu, *Electrochim. Acta* 71 (2012) 194-200.
- [49] J.C. Guo, A. Sun, X.L. Chen, C.S. Wang, A. Manivannan, *Electrochim. Acta* 56 (2011) 3981-3987.



**Huajun Tian** received his B.S. degree in China University of Geosciences (Wuhan) and earned his Ph.D. degree in Materials Physics and Chemistry from the Institute of Plasma Physics, Chinese Academy of Science, in 2013. From 2012 to 2014, he conducted postdoctoral research in Professor Weiqiang Han's research group at Ningbo Institute of Materials Technology and Engineering (NIMTE), Chinese Academy of Science. His research interests are energy storage devices, including Lithium-ion batteries and Sodium ion batteries.



**Xiaojian Tan** is currently a postdoctoral researcher at Ningbo Institute of Materials Technology and Engineering (NIMTE), Chinese Academy of Science. He received his B.S. and Ph.D. degrees from Wuhan University in 2008 and 2013. His main research interest is application of first-principles and related methods to study the structural, electronic, thermal, and other physical properties of high-performance thermoelectric materials.



**Fengxia Xin** is currently a Ph.D. candidate at Ningbo Institute of Materials Technology and Engineering (NIMTE), Chinese Academy of Science. She obtained her B.S. degree from China Jiliang University in China in 2012. Her research interests are mainly on nanomaterials for energy storage in Li-ion and Na-ion batteries.



**Dr. Chunsheng Wang** is an Associate Professor in the Chemical & Biomolecular Engineering at the University of Maryland. He received Ph.D. in Materials Science & Engineering from Zhejiang University, China, in 1995. Prior to joining the University of Maryland in 2007, he was an assistant professor in the Department of Chemical Engineering at Tennessee Technological University (TTU) in the period 2003-2007 and a research scientist at the Center for Electrochemical System and Hydrogen Research at Texas A&M University in the period 1998-2003. His research focuses on rechargeable batteries and fuel cells. Dr. Wang is the recipient of the A. James Clark School of Engineering Junior Faculty Outstanding Research Award in the University of Maryland in 2013. Details can be found at: [www.cswang.umd.edu](http://www.cswang.umd.edu).



**Wei-Qiang Han** is currently a professor and the director of the Institute of New Energy Technology at the Ningbo Institute of Materials Technology and Engineering (NIMTE), Chinese Academy of Science. He has published more than 100 papers in peer-reviewed journals. He has been developing novel nanomaterials for the applications of renewable energies, especially for advanced lithium batteries and catalysts.